InOCl nanosheets with exposed {0 0 1} facets: Synthesis, electronic structure and surprisingly high photocatalytic activity

Qian Liang[a], Hua Zhao[a], Lichao Ning[b], Jinlei Wang[a], Congjie Zhang[b], lin Wang[a], Aihua Wei[a], Qing Zhao[a], Heqing Yang[a,*], Shengzhong liu[c]

[a] Key Laboratory of Macromolecular Science of Shaanxi Province, School of Materials Science and Engineering, Shaanxi Normal University, Xi'an 710119, China
[b] Key Laboratory of Macromolecular Science of Shaanxi Province, School of Chemistry and Chemical Engineering, Shaanxi Normal University, Xi'an 710119, China
[c] Key Laboratory Applied Surface and Colloid Chemistry, Ministry of Education, School of Materials Science and Engineering, Shaanxi Normal University, Xi'an 710119, China

ARTICLE INFO

ABSTRACT

A single-crystalline InOCl nanosheet was synthesized by heating aqueous $InCl_3$ solution on a Si wafer to 400 °C. The as-synthesized InOCl nanosheets are single crystalline, grow along the directions perpendicular to (0 1 0), (2 0 0) facets of the orthorhombic InOCl and are enclosed by {0 0 1} top and down surfaces. Their typical widths, lengths and thicknesses are in the range of 1.4 to 2.5 μm, 8.4 to 16.7 μm, and 42 to 71 nm, respectively. The InOCl nanosheets with exposed {0 0 1} facets show higher photocatalytic activity than Degussa P25 TiO_2 for degradation of organic dyes. The calculated band structure of InOCl confirms that it has an indirect band-gap. The highest occupied orbital is hybridization of Cl 3p and O 2p states, and the In 5s state dominates the lowest unoccupied orbital. The crystal structure of InOCl is shown, and its excellent photocatalytic activity was attributed to their open crystal structure and indirect optical transitions.

1. Introduction

Recently, considerable attention has been paid to the morphology and crystal-facet-controlled fabrication of semiconductor nanomaterials because of their facet-dependent photocatalytic, gas-sensing and photoelectric properties [1–3]. Yang et al. synthesized anatase TiO_2 crystals with exposed {0 0 1} facets by using hydrofluoric acid as a capping agent [4] and found that the TiO_2 nanosheets having {0 0 1} facets show superior photocatalytic activity compared with P25 as a benchmarking material [5]. Subsequently, it was reported that TiO_2 flower-like microspheres with exposed {0 0 1} facets [6], $BiVO_4$ nanoplates with exposed {1 0 0} facets [7], BiOCl [8], WO_3 [9] and β-Bi_2O_3 nanosheets [10] with exposed {0 0 1} facets, Ag_3PO_4 rhombic dodecahedrons with exposed {1 1 0} facets [11], hexagram shaped InOOH nanostructures with exposed {0 2 0} facets [12], flowerlike nanoarchitectures assembled CdS nanosheets with exposed {0 0 1} facets[13], NiO [14] and Cu_2O [15] octahedrons with exposed {1 1 1} facets, and 50-facet polyhedral Cu_2O with high-index{5 2 2} facets [16] exhibited enhanced photocatalytic activity for the degradation of toxic organic pollutants [6–16]. $ZnIn_2S_4$ Persimmon-like microspheres with exposed {0 0 6} facets [17] and TiO_2 nanosheets with exposed {0 0 1} facets [18] exhibited enhanced photocatalytic activity for the production of H_2 from water splitting. The Bi_2WO_6 sheets with the preferentially exposed {0 0 1} facets exhibited greatly enhanced photocatalytic activity for reduction of CO_2 into renewable hydrocarbon fuel [19]. The SnO_2 octahedral nanoparticles with exposed {2 2 1} facets exhibited better gas-sensing performance over ethanol than those mainly having exposed {1 1 0} facets [20]. Although these highly reactive facets are more interesting and important for improving photocatalytic and gas-sensing properties, they usually diminish rapidly during the crystal growth process as a result of the minimization of surface energy. To address this issue, organic polymers or inorganic ions have usually been employed for selective control of the growth rates of various planes [1–4,12–14]. However, the percentage of highly reactive facets in the final products has still been relatively low. In addition, capping agents adsorbed on the surfaces of semiconductor crystals must be removed by complex treatments before their catalytic applications and the highly reactive facets may lose many of their active sites

* Corresponding author. Tel.: +86 029 81530710; fax: +86 029 81530702.
E-mail address: hqyang@snnu.edu.cn (H. Yang).

as a result of surface reconstruction. Thus, the fabrication of semiconductor nanocrystals with only highly reactive facets exposed and without capping agents is still a great challenge. To the best of our knowledge, the superior photoreactivity of indium oxychloride with exposed {0 0 1} facets have never been reported until now.

Herein, we report on the synthesis of InOCl nanosheets with {0 0 1} surfaces by heating InCl$_3$ solution on a Si substrate. Photocatalytic activities of the as-prepared InOCl nanosheets in the degradation of Malachite Green with a molecular weight of 927.00 (MG), rhodamine B (RhB) and methyl orange (MO) were investigated. Moreover, to understand the electronic structure of InOCl, theoretical calculations were performed using a density functional method. The crystal structure of InOCl is shown, and the structure–property relationship was discussed in detail.

2. Experimental

2.1. Preparation

All reagents used were of analytical grade and were directly used as received without any further purification. 0.510 M aqueous solution of InCl$_3$ was obtained by dissolving 15.000 g of InCl$_3$·4H$_2$O in 100.0 ml of 0.12 M hydrochloric acid.

The InOCl nanosheets were prepared as follows: In a typical experiment, a silicon substrate (1 × 1 cm) was cleaned in deionized water and absolute ethanol with ultrasonic irradiation for 15 min, respectively. Two drops of 0.510 M InCl$_3$ aqueous solution were added onto a silicon substrate in a quartz boat. The boat was positioned in a conventional box furnace. The furnace was heated to 280 °C at a rate of 20 °C/min, maintained at the temperatures for 2 h, then was switched off, and cooled to room temperature naturally. The furnace was heated to 400 °C at a rate of 20 °C/min again, then, was switched off, and cooled to room temperature naturally. A large amount of white products were grown on the Si substrate.

2.2. Characterization

The as-prepared products were characterized and analyzed using powder X-ray diffraction (XRD), scanning electron microscopy (SEM), and transmission electron microscopy (TEM). The XRD analysis was performed using a Rigaku DMX-IIIC X-ray diffractometer with Cu $K\alpha_1$ radiation ($\lambda = 1.541$ Å) at 40 kV and 100 mA. Each specimen was scanned at a step size of 0.02° and a scanning speed of 8°/min with diffraction angles varying between 5° and 80°. SEM images were obtained on a FEI Quanta 200 scanning electron microscope at an accelerating voltage of 20 kV. TEM and electron diffraction images were obtained using a JEOL JEM-3100 transmission electron microscope at an accelerating voltage of 300 kV. The samples for TEM were prepared by dispersing a powder scraped from the original sample on a carbon-coated copper grid. The specific surface area was measured by nitrogen adsorption/desorption using Brunauer–Emmett–Teller (BET) method on a Quadrasorb SI-3 Surface and Porosimetry Analyzer (Quantachrome, USA). UV–vis diffuse reflectance spectrum of the products was conducted on a Perkin Elmer Lambd 950 UV–visible-NIR spectrophotometer.

2.3. Evaluation of photocatalytic activity

MG, RhB and MO were selected as model organic compounds to examine the photocatalytic activity of the InOCl nanosheets. 10.0 mg of the as-prepared photocatalysts was added to 10.0 ml of 1.0×10^{-5} M MG, 1.0×10^{-5} M RhB or 5.0×10^{-5} M MO solution to get a suspension. The suspension was magnetically stirred for 15 min in the dark to establish an adsorption/desorption equilibrium between the dye and the photocatalysts. Then the mixed
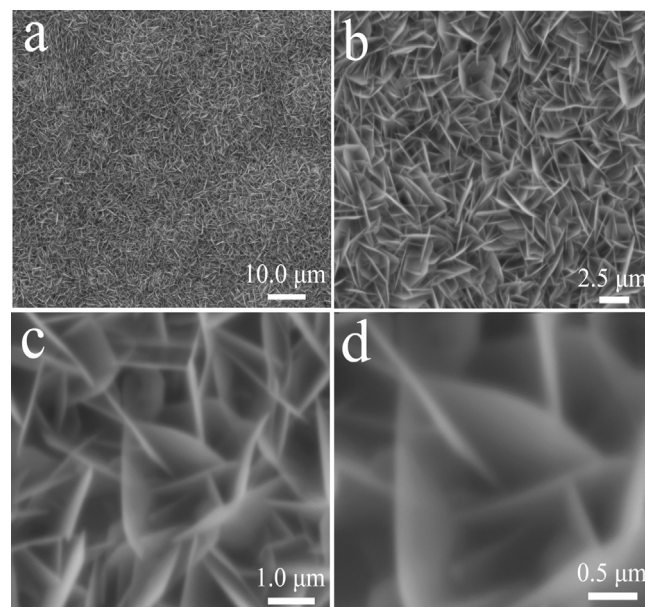

Fig. 1. SEM images of the products grown on the Si substrate.

solution was irradiated with a 500 W medium-pressure mercury-vapor lamp at a distance of about 8 cm (XPA-7 photochemical reactor, Xujiang Electromechanical Plant, Nanjing, China). At a given irradiation time interval, 5 ml of sample was withdrawn from the test tube for analysis. Sample solutions were obtained by centrifugation, and their absorption spectra were measured by on a Hitachi U-2910 ultraviolet–visible spectrophotometer using deionized water as reference. For comparison, the photocatalytic activities of commercial TiO$_2$ (Degussa P25) were also tested under the same reaction conditions and with the equal catalyst weight as that employed for InOCl.

3. Results and discussion

3.1. Morphology and crystal structure

The morphology and crystal structure of the as-prepared samples were investigated by SEM and XRD, and the results are shown in Figs. 1 and 2. Fig. 1 shows typical SEM images of the samples, which reveals that a large-scale sheet-like structures cover on the Si substrate. The nanosheets have widths of 1.4 to 2.5 μm and
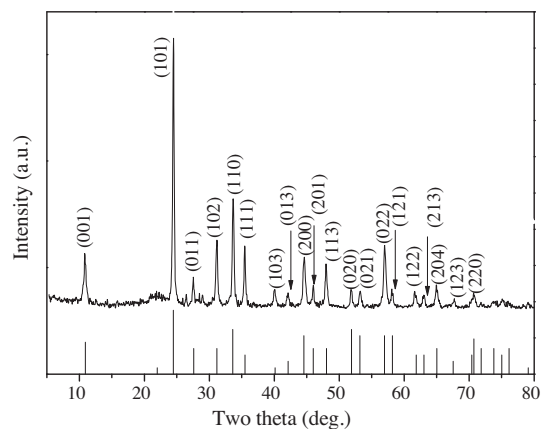

Fig. 2. XRD pattern of the products grown on the Si substrate. The stick patterns is the standard XRD pattern of orthorhombic InOCl powders from the Joint Committee on Power Diffraction Standards (JCPDS card no. 11-0510).
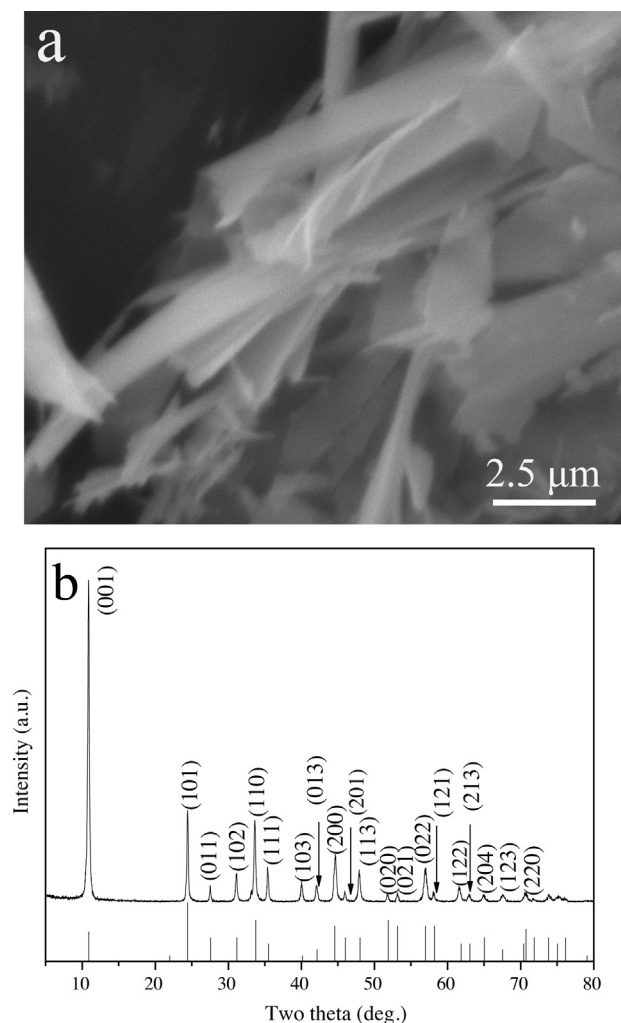
Fig. 3. SEM image (a) and XRD pattern (b) of the InOCl nanosheets removed from the Si substrate.

thickness of 42 to 71 nm. These nanosheets intercross with each other to form a network structure. Fig. 2 exhibits XRD pattern of the as-obtained nanosheet networks. All the diffraction peaks of the XRD patterns could be perfectly indexed to pure orthorhombic InOCl (Joint Committee on Powder Diffraction Standards (JCPDS) card no. 11-0510), suggesting that the sheet-like nanostructures are InOCl with an orthorhombic structure. The InOCl nanosheets were removed from the Si substrate, and characterized by SEM and XRD. SEM image shown in Fig. 3a reveal that the products consist of a large quantity of sheet like nanostructures. The typical lengths, widths and thickness of the InOCl nanosheets are in the range of 8.4 to 16.7 µm, 1.4 to 2.5 µm, 42 to 71 nm, respectively. In the XRD pattern shown in Fig. 3b, the higher intensity ratios of (0 0 1) to other diffraction peaks in comparison with those in Fig. 2 and in the corresponding standard pattern of orthorhombic InOCl are observed, which suggests that the InOCl nanosheets are primarily dominated by {0 0 1} facets.

The texture coefficient (TC) of (0 0 1) plane is defined as [21]

$$TC(0\ 0\ 1) = \frac{I(0\ 0\ 1)}{I_0(0\ 0\ 1)}\left\{\frac{1}{n}\sum\frac{I(h\ k\ l)}{I_0(h\ k\ l)}\right\}^{-1} \qquad (1)$$

where $I(h\,k\,l)$ are measured intensities of $(h\,k\,l)$ reflection, $I_0(h\,k\,l)$ are powder diffraction intensities of orthorhombic InOCl according to the JCPDS Card No. 11-0510, and n is the number of diffraction peaks used in the calculations. For materials with random crystallographic orientations, e.g. powders, the texture coefficient is 1. The

TC of (0 0 1) diffraction peaks for the as-obtained samples is 9.3, which indicates that the nanosheets may be enclosed by ±(0 0 1) top and bottom surface.

To further illuminate the detailed structure of the InOCl nanosheets, the products removed from the Si substrate were characterized using TEM, and the results are shown in Fig. 4. Fig. 4a presents typical TEM image of the InOCl sheet like structures. The InOCl nanosheets have smooth surfaces, widths of 2.0 to 2.4 µm and lengths of 5.2 to 5.5 µm, which is consistent with the SEM observation. A ripple like contrast observed in the TEM image is due to strain resulting from the bending of the sheets. Fig. 4(b) and (c) show selected area electron diffraction (SAED) pattern and high-resolution TEM (HRTEM) image from box in (a), respectively. The SAED pattern can be indexed to [0 0 1] zone axis of orthorhombic phase InOCl. The lattice spacings of 0.17 and 0.20 nm can be observed clearly from the HRTEM image, which correspond to (0 2 0) and (2 0 0) facets, respectively. Both the SAED and the HRTEM results indicate that the InOCl nanosheets are single crystalline, grow along the directions perpendicular to (0 2 0), (2 0 0) facets of the orthorhombic InOCl and are enclosed by {0 0 1} top and down surfaces.

3.2. Band structure of InOCl

The band structure of InOCl was calculated by using the generalized gradient approximation (GGA) with Perdew–Burke–Ernzerhof (PBE) functional in DMol[3] of the Material Studio Package [22,23]. The Brillouin zone was sampled with a Monkhorst–Pack k-point grid of $6 \times 6 \times 3$. The band structure of InOCl is displayed in Fig. 5. The conduction-bond bottom is located at the Γ (0, 0, 0) point, but the valence-band top is found near the S (−0.5, 0.5, 0) and R (−0.5, 0.5, 0.5) points, showing an indirect nature of the band-gap nature of InOCl. The total and partial electronic density of states (DOS) of InOCl are shown in Fig. 6. The order of the states from −20 to 15 eV starts with mainly O 2s states (−17.5 to −11.6 eV), then localized In 4d states (−17.3 to −11.5 eV), Cl 3s (−14.6 to −11.5 eV), O 2p and Cl 3p (−5 to 0 eV), In 5s (2.8–6.5 eV) and In 5p (5.0 to 13.2 eV). The Cl 3p and O 2p states contribute considerably to the DOS beneath the Fermi level, whereas the In 5s and 5p states just make significant contribution above the Fermi level. The valence-bond is mainly O 2p and Cl 3p states, and the conduction-band is mainly In 5s state. However, some O 2p and Cl 3p states appear above the Fermi level (5–12.5 eV), and some In 5s state appears from −5 to 0 eV. Also, the Cl 3p, O 2p and In 5s states exhibit a peak in the same point (about 5.6 eV). The results indicate that In 5s, O 2p, and Cl 3p states hybridize slightly. The highest occupied orbital (HOMO) is hybridization of Cl 3p and O 2p states. The In 5s state dominates the lowest unoccupied orbital (LUMO).

3.3. UV–vis diffuse reflectance spectroscopy

UV–vis diffuse reflectance spectrum of the InOCl powders is shown in Fig. 7. The as-prepared BiOCl nanosheets display a white color, the onset of InOCl is determined at 254 nm and the absorption edge occurs at about 320 nm. As a crystalline semiconductor, the optical absorption near the band edge follows the formula,

$$\alpha h\nu = A(h\nu - E_g)^{n/2}$$

where, α, ν, E_g, and A are the absorption coefficient, light frequency, band gap energy, and a constant, respectively [24,25]. Among them, n depends on the characteristics of the transition in a semiconductor, i.e., direct transition ($n = 1$) or indirect transition ($n = 4$). For InOCl, the value of n is 4 for the indirect transition. The band gap energy (E_g value) of InOCl can be thus estimated from a plot of
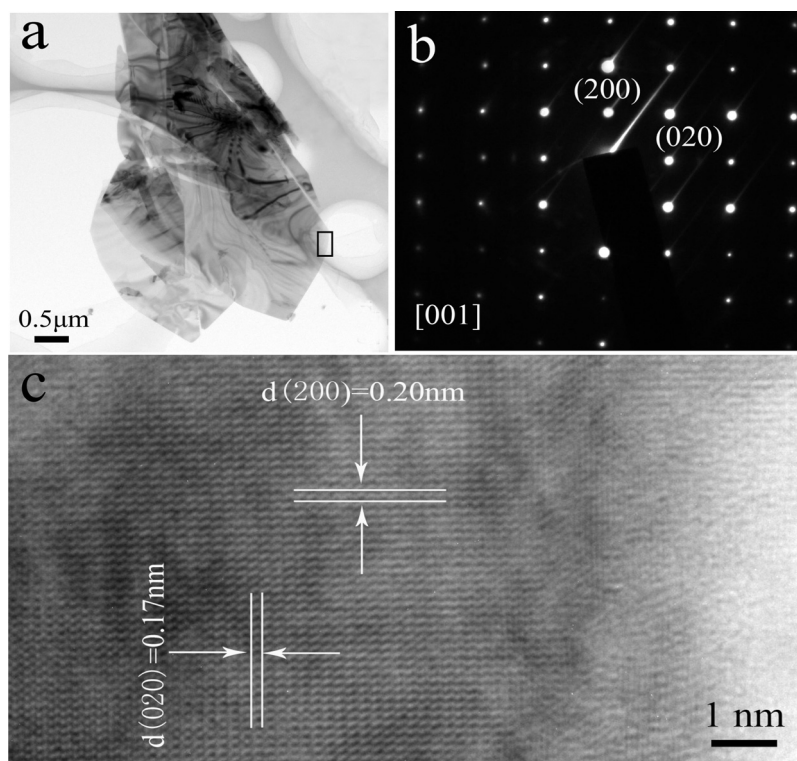
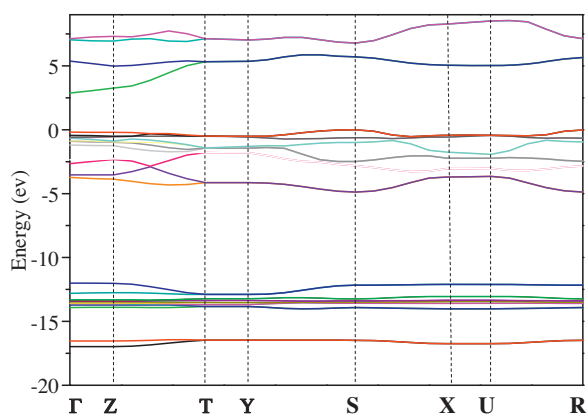**Fig. 4.** TEM (a), SAED (b) and HRTEM (c) images of the as-obtained InOCl nanosheets.

Fig. 5. Band structure of InOCl. The high-symmetry points are Γ (0, 0, 0), Z (0, 0, 0.5), T (−0.5, 0, 0.5), Y (−0.5, 0, 0), S (−0.5, 0.5, 0), X (0, 0.5, 0), U (0, 0.5, 0.5), R (−0.5, 0.5, 0.5), respectively.
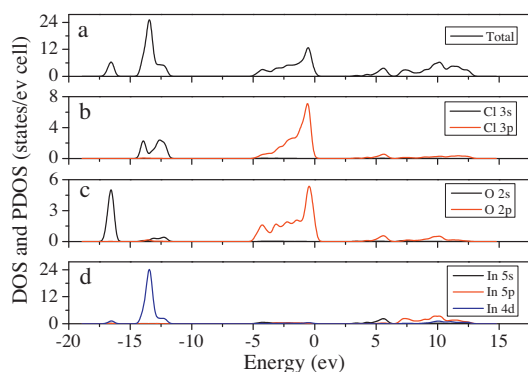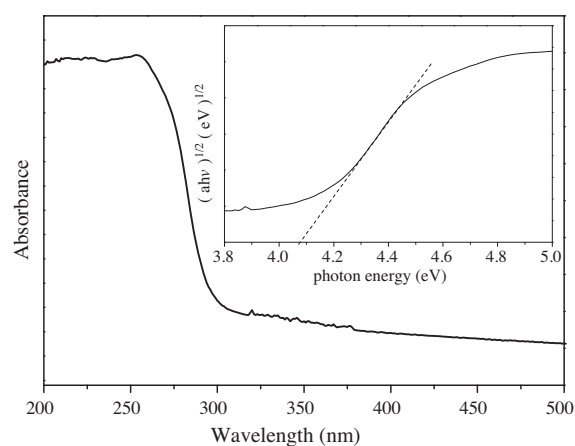

Fig. 7. UV–vis diffuse reflectance spectrum of the InOCl nanosheets. Illustrations is the plot of $(\alpha h\nu)^{1/2}$ versus photon energy (hν) for the InOCl nanosheets.

Fig. 6. Total DOS of InOCl (a), and Cl (b), O (c) and In (d) DOS.

$(\alpha h\nu)^{1/2}$ versus photon energy ($h\nu$) (inset in Fig. 7), and the result is found to be about 4.08 eV.

3.4. Photocatalytic activity

To demonstrate the potential applicability in photocatalysis of the as-obtained InOCl nanosheets, we investigated their photocatalytic activity in the degradation of MG, RhB and MO. The absorption spectra of MG, RhB and MO aqueous solutions under different conditions were measured, and the results are shown in Fig. 8. MG, RhB and MO show a maximum absorption band at 616, 552 and 462 nm, respectively (curve I in Fig. 8a–c. After absorption for 15 min, the absorption intensity of the MG, RhB and MO peaks is reduced by about 5.6, 8.3 and 26%, respectively. In addition, the MO absorption peak is shifted from 462 to 480 nm. In the presence of
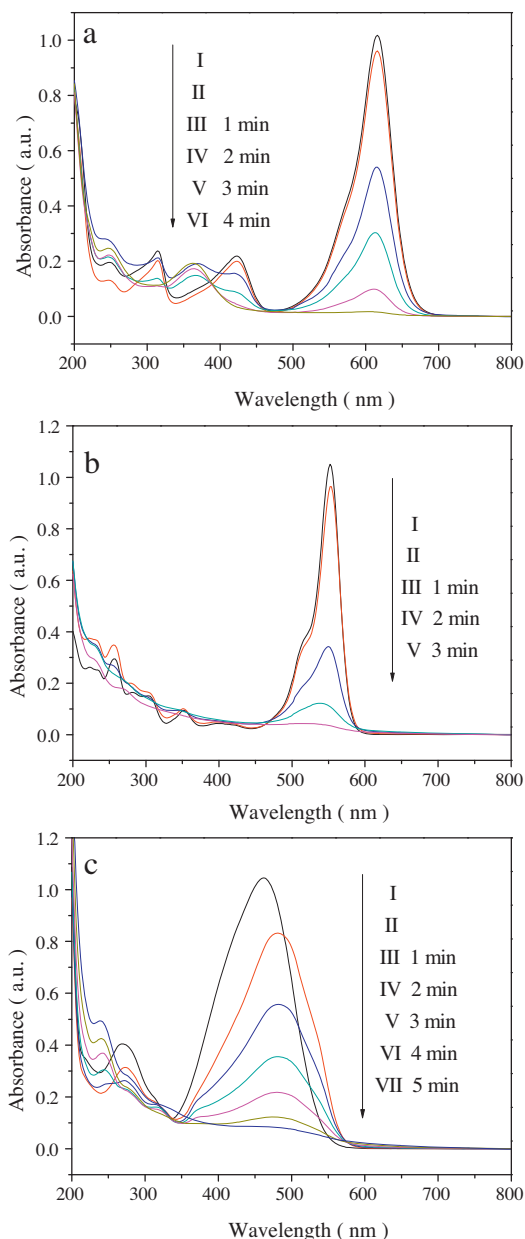
Fig. 8. (a) Absorption spectra of (I) MG stock solution, (II) MG solution after 15 min adsorption by InOCl nanosheets and (III–VI) MG solution during the photocatalytic degradation process over InOCl nanosheets. (b) Absorption spectra of (I) RhB stock solution, (II) RhB solution after 15 min adsorption by InOCl nanosheets and (III–V) RhB solution during the photocatalytic degradation process over InOCl nanosheets. (c) Absorption spectra of (I) MO stock solution, (II) MO solution after 15 min adsorption by InOCl nanosheets and (III–VII) MO solution during the photocatalytic degradation process over InOCl nanosheets.

InOCl nanosheets, after UV light irradiation for 1 min, the absorption intensity of the MG, RhB and MO peaks is reduced by about 44, 65 and 33%, respectively. The MG, RhB and MO absorption peaks completely disappeared after irradiation for 4, 3 and 5 min, respectively. The reduction of absorbance may be due to the destruction of the dye chromogen. Since no new peak was observed, these organic dyes may be decomposed. The results reveal that the InOCl nanosheet is a very effective photocatalyst for the degradation of organic dyes.

We selected the characteristic absorption peaks of MG, RhB and MO for monitoring the photocatalytic degradations over P25 and InOCl nanosheets. Fig. 9a–c show the decomposition of MG, RhB and MO in solutions over P25 (curve II) and InOCl nanosheets (curve III)
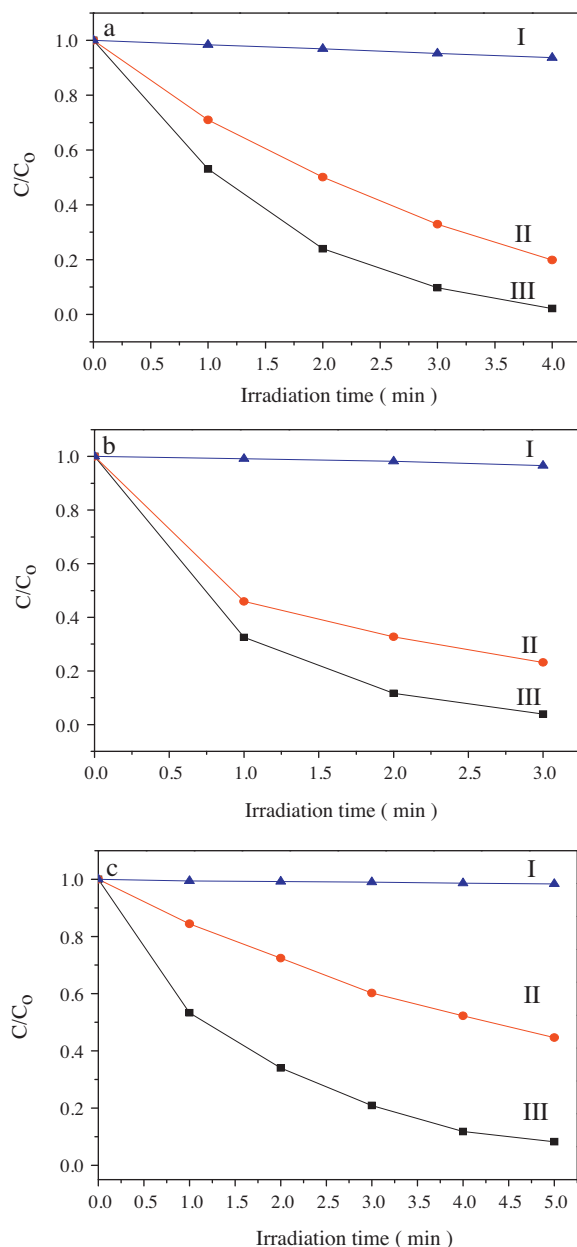

Fig. 9. Photodegradation of the (a) MG, (b) RhB and (c) MO solutions without catalyst (I), over Degussa P25 TiO_2 powders (II) and the InOCl nanosheets (III) under UV light irradiation.

under mercury lamp irradiation as a function of time, respectively. It can be clearly seen that the decomposition of the MG, RhB and MO progress relaxedly without catalyst. However, the MG, RhB and MO decompositions over the catalysts progress fleetly, and the rate of MG, RhB and MO dye decompositions over the InOCl nanosheets is faster than that over P25. The fittings of $\ln(C_0/C)$ plot versus time over P25 and InOCl nanosheets for MG, RhB and MO are shown in Fig. 10. The photodegradations of MG, RhB and MO catalyzed by both the catalysts fit pseudo first-order reaction. i.e. $\ln(C_0/C) = Kt$, K is the apparent rate constant of the degradation. In our experiment, the measured K values were listed in Table 1. The results imply that the as-prepared InOCl nanosheets show higher photocatalytic activity than P25 for degradation of MG, RhB and MO.

It is generally accepted that the catalytic process is mainly related to the adsorption and desorption of molecules on the surface of the catalyst. BET surface area of the InOCl nanosheets and
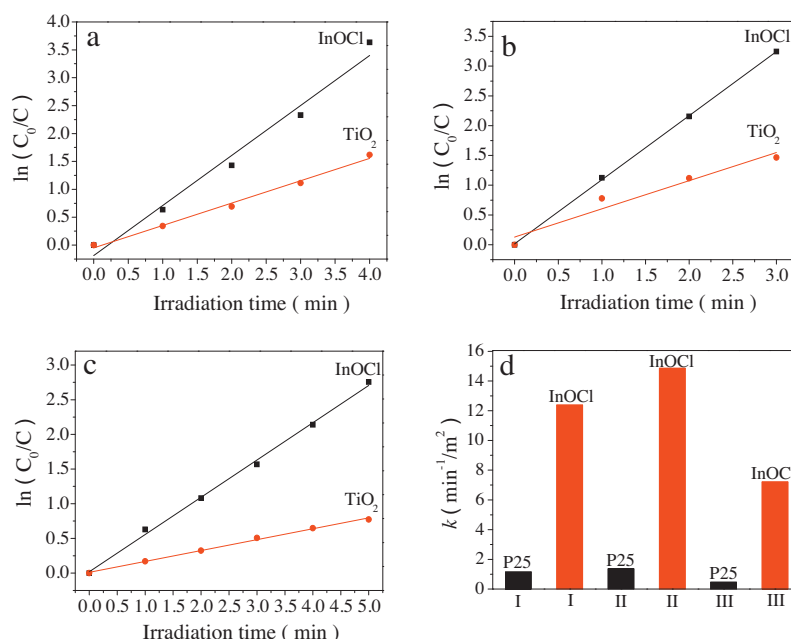
Fig. 10. The fittings of $\ln(C_0/C)$ plot versus time over P25 and the InOCl nanosheets for (a) MG, (b) RhB and (c) MO. (d) Normalized apparent rate constants of the MG, RhB and MO degradation per unit surface area (k) over P25 and the InOCl nanosheets.

Table 1
The apparent rate constants of the MG, RhB and MO degradation [K (min^{-1})] of P25 and the InOCl nanosheets.

	MG	RhB	MO
InOCl	0.897 ± 0.072	1.076 ± 0.012	0.522 ± 0.016
P25	0.401 ± 0.020	0.473 ± 0.075	0.164 ± 0.003

Table 2
The apparent rate constants of the MG, RhB and MO degradation per unit surface area [k (min^{-1}/m^2)] of P25 and the InOCl nanosheets.

	MG	RhB	MO
InOCl	12.379	14.861	7.204
P25	1.147	1.355	0.469

P25 was measured to be 7.2 and 34.9 m^2/g, respectively. The apparent rate constants of the MG, RhB and MO degradations per unit surface area of the both catalysts, as for the basis for the comparison, are examined in this work. Whether degradations of MG, RhB or MO, the normalized K value (k) of InOCl nanosheets is higher than that of Degussa P25 TiO$_2$, as seen in Fig. 10d and Table 2. The results clearly demonstrate that the photocatalytic activity of the as-prepared InOCl nanosheets show superior photocatalytic activity compared with Degussa P25 TiO$_2$. To test the repeatability of organic dye bleaching on the InOCl nanosheets, we carried out the MG bleaching experiment repeatedly four times by using the InOCl nanosheets as the photocatalysts. As shown in Fig. 11 their photocatalytic activity was lightly lowered after four cycles, which indicated that the as-prepared InOCl nanosheets exhibit remarkable photocatalytic stability.

3.5. Structure–property relationship

Excellent photocatalytic activity of InOCl may be attributed to its peculiar electronic structure as an indirect band gap semiconductor. The crystal structure of InOCl view along [0 0 1] and [1 0 0] is displayed in Fig. 12, and its lattice parameters is optimized to
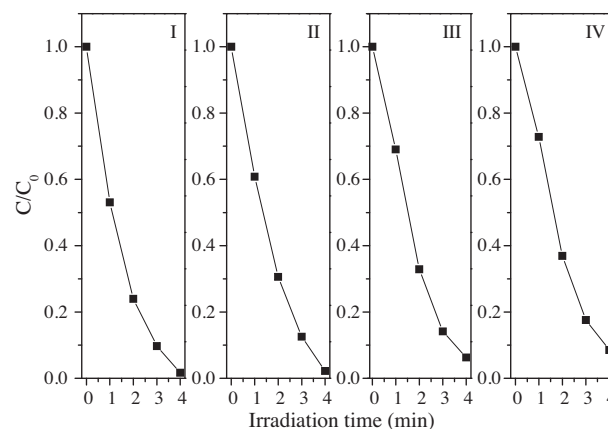

Fig. 11. Cyclic photodegradation of the MG solution with the InOCl nanosheets under UV light irradiation.

be $a = 0.4186$, $b = 3.608$ and $c = 8.789$ nm. The In atom is coordinated to a square antiprism with four O atoms in one base and two Cl atoms in another (Fig. 12a). The Cl atom is bonded with two neighboring In atoms in a line to form a triangle and with its nonbonding (lone pair) electrons pointing to the other side of the triangle (Fig. 12a and b). The O atom is tetrahedrally coordinated to four In atoms (Fig. 12b). These nonbonding electrons convert the three-dimensional fluorite-like structure into a two dimensional layered structure.

As shown in Fig. 12, the [InOCl] layers are stacked together by the nonbonding (van der Waals) interaction through the Cl atoms along the c-axis. Therefore, the structure is not closely packed in this direction. When one photon excites one electron from Cl 3p states to In 5s states in InOCl, one pair of a hole and an excited electron appear. The layered structure InOCl can provide the space large enough to polarize the related atoms and orbitals. The induced dipole can separate the hole–electron pair efficiently, enhancing photocatalytic activities [26]. In addition, InOCl has an indirect-transition band-gap so that the excited electron has to travel certain
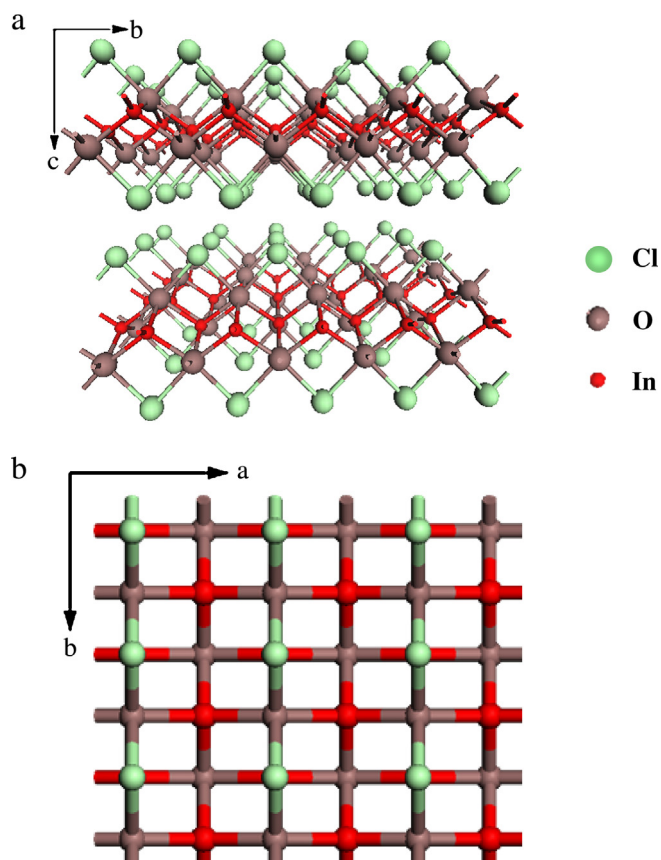
- Cl
- O
- In

Fig. 12. The crystal structure of InOCl viewed along [1 0 0] (a) and [0 0 1] (b).

k-space distance to be emitted to valence band [26,27]. This reduces the recombination probability of the excited electron and the hole. Both the open (loose packed) structure and indirect transitions may benefit the hole–electron separation and the charge transport. Thus, these features are both favorable to the photocatalytic reactions.

4. Conclusions

In summary, InOCl nanosheets with {0 0 1} surfaces was synthesized through heating aqueous InCl₃ solution to 400 °C. The as-synthesized InOCl nanosheets was investigated as a photocatalyst for the first time, and was found to show higher photocatalytic activity than Degussa P25 TiO₂ for degradation of organic dyes. The

electronic structure of InOCl calculated at the GGA/PBE/DNP level shows that InOCl has an indirect-transition band-gap. The highest occupied orbital is hybridization of Cl 3p and O 2p states, and the In 5s state dominates the lowest unoccupied orbital. The crystal structure of InOCl is shown, its open crystal structure and indirect optical transitions play important roles in its excellent photocatalytic activity. The results suggest that other layered compounds, such as TiOCl and FeOCl may exhibit good photocatalytic activity, and provides opportunities for both fundamental research and technological applications.

References

[1] H. Tong, S.X. Ouyang, Y.P. Bi, N. Umezawa, M. Oshikiri, J.H. Ye, Adv. Mater. 24 (2011) 229–251.
[2] Z.Y. Jiang, Q. Kuang, Z.X. Xie, L.S. Zheng, Adv. Funct. Mater. 20 (2010) 3634–3645.
[3] K.B. Zhou, Y.D. Li, Angew. Chem. Int. Ed. 51 (2012) 602–613.
[4] H.G. Yang, C.H. Sun, S.Z. Qiao, J. Zou, G. Liu, S.C. Smith, H.M. Cheng, G.Q. Lu, Nature. 453 (2008) 638–641.
[5] H.G. Yang, G. Liu, S.Z. Qiao, C.H. Sun, Y.G. Jin, S.C. Smith, J. Zou, H.M. Cheng, G.Q. Lu, J. Am. Chem. Soc. 131 (2009) 4078–4083.
[6] Q.J. Xiang, J.G. Yu, M. Jaroniec, Chem. Commun. 47 (2011) 4532–4534.
[7] G.C. Xi, J.H. Ye, Chem. Commun. 46 (2010) 1893–1895.
[8] J. Jiang, K. Zhao, X.Y. Xiao, L.Z. Zhang, J. Am. Chem. Soc. 134 (2012) 4473–4476.
[9] D.Q. Zhang, S.L. Wang, J. Zhu, H.X. Li, Y.F. Lu, Appl. Catal., B 123–124 (2012) 398–404.
[10] H. Liu, M. Luo, J.C. Hu, T.F. Zhou, R. Chen, J.L. Li, Appl. Catal., B 140–141 (2013) 141–150.
[11] L.Q. Ye, L. Zan, L.H. Tian, T.Y. Peng, J.J. Zhang, Chem. Commun. 47 (2011) 6951–6953.
[12] H. Zhao, W.Y. Yin, M.Y. Zhao, Y.Z. Song, H.Q. Yang, Appl. Catal., B 130–131 (2013) 178–186.
[13] R. Jin, M.Y. Su, J. Wang, P. Zhang, M. Cui, Y. Chen, H.Q. Yang, Mater. Res. Bull. 47 (2012) 3070–3077.
[14] B. Liu, A.H. Wei, J.Y. Zhang, L.J. An, Q.Q. Zhang, H.Q. Yang, J. Alloys Compd. 544 (2012) 55–61.
[15] C.H. Kuo, M.H. Huang, J. Phys. Chem. C 112 (2008) 18355–18360.
[16] S.D. Sun, X.P. Song, Y.X. Sun, D.C. Deng, Z.M. Yang, Catal. Sci. Technol. 2 (2012) 925–930.
[17] J. Shen, J.T. Zai, Y.P. Yuan, X.F. Qian, Int. J. Hydrogen Energy 37 (2012) 16986–16993.
[18] G. Liu, C.H. Sun, H.G. Yang, S.C. Smith, L.Z. Wang, G.Q. Lu, H.M. Cheng, Chem. Commun. 46 (2010) 755.
[19] Y. Zhou, Z.P. Tian, Z.Y. Zhao, Q. Liu, J.H. Kou, X.Y. Chen, J. Gao, S.C. Yan, Z.G. Zou, ACS Appl. Mater. Interfaces 3 (2011) 3594–3601.
[20] X.H. Han, M.H. Jin, S.F. Xie, Q. Kuang, Z.Y. Jiang, Y.Q. Jiang, Z.X. Xie, L.S. Zheng, Angew. Chem. Int. Ed. 121 (2009) 9344–9347.
[21] S.P. Harimkar, N.B. Dahotre, J. Appl. Phys. 100 (2006) 024901.
[22] B. Delley, J. Chem. Phys. 92 (1990) 508–517.
[23] B. Delley, J. Chem. Phys. 113 (2000) 7756–7764.
[24] M.A. Butler, J. Appl. Phys. 48 (1977) 1914–1920.
[25] X. Zhang, Z.H. Ai, F.L. Jia, L.Z. Zhang, J. Phys. Chem. C 112 (2008) 747–753.
[26] K.L. Zhang, C.M. Liu, F.Q. Huang, C. Zheng, W.D. Wang, Appl. Catal., B 68 (2006) 125–129.
[27] A. Hagfeldt, M. Gratzel, Chem. Rev. 95 (1995) 49–68.